Engineering Geology 243 (2018) 241–252

Contents lists available at ScienceDirect

Engineering Geology

journal homepage: www.elsevier.com/locate/enggeo

Complex-conductivity imaging for the understanding of landslide architecture

Adrián Flores Orozco[a,*], Matthias Bücker[a], Matthias Steiner[a,b], Jean-Philippe Malet[c]

[a] Geophysics Research Division, Department of Geodesy and Geoinformation, TU-Wien, Vienna, Austria
[b] Institute of Applied Geology, University of Natural Resources and Life Sciences, Vienna, Austria
[c] Institut de Physique du Globe de Strasbourg, CNRS UM7516, University of Strasbourg/EOST, Strasbourg, France

A B S T R A C T

Geophysical methods are widely used for landslide investigation to delineate depth and geometry of the sliding plane. In particular, electrical resistivity tomography (ERT) is often used because both porosity and water saturation control the electrical resistivity of the subsurface materials and are critical for slope stability. Moreover, ERT can be employed to monitor changes in pore-fluid pressure which is an important factor triggering landslides. However, the interpretation of ERT results in clay-rich landslides can be challenging considering that high electrical conductivity values may not only be related to an increase in saturation but also to the surface conduction mechanism, which becomes dominant in the presence of clays. Recently, environmental investigations have demonstrated an improved subsurface characterization through induced polarization (IP) imaging, an extension of the ERT method, which permits to gain information about electrical conductive and capacitive (i.e., polarization effect) properties of the subsurface. As the polarization effect is mainly controlled by surface charge, which is large in clays, IP images are expected to improve the lithological interpretation and overcome the limitations of the ERT method. Additionally, measurements collected over a broad frequency bandwidth, the so-called spectral IP (SIP), have been successfully used in laboratory experiments to quantify textural and hydrogeological parameters. However, the application of SIP field measurements for the delineation of hydrogeological structures in landslides has not been addressed to date. To fill this gap, in this study we present SIP imaging results for data collected at the La Valette landslide (South East French Alps), where an existing geotechnical model of the landslide is available for evaluation. Moreover, our study provides a detailed revision on the collection and processing of SIP datasets, as well as a description of the diverse sources of error in IP surveys, to stress the importance of data-error quantification for a quantitative application of the SIP method. Our results demonstrate that adequate data processing allows obtaining consistent results at different frequencies and independently of the measuring protocol. Furthermore, the frequency dependence of the complex conductivity obtained in the field-scale SIP survey is consistent with earlier laboratory experiments. In conclusion, our study shows the potential of the SIP method to improve our understanding of subsurface properties, and an improved delineation of the contact between the mobilized material and the bedrock as well as variations in the clay content within the landslide and the bedrock.

1. Introduction

Landslides pose a high geological hazard on human settlements, infrastructure, and agricultural areas. One of the most important processes triggering landslides refers to the increase in pore-fluid pressure, for instances following intense rainfall events (Samyn et al., 2012; Brückl et al., 2013). Hence, a characterization of the internal structure and geometry of landslides with high spatial resolution is critical to identify preferential groundwater flow paths as well as clay-rich areas, where water could accumulate. Such information is critical in the management and control of landslides, taking into account that climate change models predict an increase of rainfall during the winter and rainy seasons in humid regions, such as Europe (Maraun et al., 2010), and a possible increase of landsliding rates (Malet et al., 2007).

Subsurface landslide characterization is commonly performed through geological and geotechnical methods, which require drilling or trenching. Although such techniques provide direct information about deformation, lithology, water content, and geotechnical properties, their spatial resolution is often limited to the immediate vicinity of the sampling point. Furthermore, direct investigations commonly require interpolation of the data, which may lead to inaccuracies or a bias in the interpretation of the resulting investigations. Due to the increase in costs and time required for a repeated sampling and analysis, direct methods may also not be suited for monitoring purposes. The application of geophysical methods can help to overcome some of these limitations, as they permit to gain quasi-continuous spatial and temporal information about subsurface materials without disturbing the study area.

In the case of landslide investigations, seismic refraction and reflection (SRR) techniques have been used for decades to characterize the landslide internal structure, in particular the geometry of the sliding planes (e.g., Gance et al., 2012; Brückl et al., 2013). Geophysical

* Corresponding author.
E-mail address: flores@tuwien.ac.at (A. Flores Orozco).

https://doi.org/10.1016/j.enggeo.2018.07.009
Received 22 December 2017; Received in revised form 6 June 2018; Accepted 8 July 2018
Available online 10 July 2018
0013-7952/

electrical methods, such as electrical resistivity tomography (ERT), have also been applied to delineate the geometry of the sliding plane and assess lithological changes (Friedel et al., 2006; Supper et al., 2014), to estimate landslide hydrological properties (Travelletti et al., 2012; Gance et al., 2016) or to complement seismic surveys (Hibert et al., 2012; Travelletti et al., 2009). Making use of the dependency of the electrical conductivity on the water content, ERT applications have also been used to monitor water content and pore-fluid pressure, which allowed forecasting local failures leading to landslides or debris flow (Friedel et al., 2006; Travelletti et al., 2012; Supper et al., 2014). However, the interpretation of ERT results in terms of water content may be challenging. High electrical conductivity (σ) values are not always related to an increase in water saturation, through electrolytic conduction (Archie, 1942), but can also be due to a high contribution of surface conduction. Particularly in clay-rich materials, surface conduction along the microscopic solid-liquid interfaces, which are covered by an electrical double layer (EDL), might be dominant and mask the saturation dependence of the electrical conductivity (Waxman and Smits, 1968; Revil and Glover, 1998; Slater, 2006). The reader is referred to Ward (1988) for a detailed revision.

Recent hydro-geophysical investigations (Kemna et al., 2012; Binley et al., 2015; Flores Orozco et al., 2015) have demonstrated an improved understanding of lithological structures by means of the Induced Polarization (IP) imaging method, an extension of the ERT, which provides information about the conductive and capacitive (i.e., polarization) properties of the subsurface. Because the polarization effect is mainly controlled by surface charges in the EDL, IP images can help discriminating between saturated sediments and clay-rich materials and, thus, improve the estimation of hydrogeological parameters (Slater and Lesmes, 2002; Slater, 2006). From laboratory studies and theoretical modeling, it is also evident that the frequency dependence of the IP effect, which can be assessed by spectral IP (SIP) measurements, is strongly correlated with the geometrical properties of the pore space (Binley et al., 2005; Bücker and Hördt, 2013). Consequently, SIP imaging has the potential to contribute to the quantification of textural and hydrogeological parameters (Revil and Florsch, 2010) and, thus, improve the geophysical characterization of units with different hydrogeological properties in landslides.

Despite this expected potential, to date only rare studies have addressed the application of IP methods for landslide characterization (Marescot et al., 2008; Sastry and Mondal, 2012). In addition, these studies did not discuss the frequency dependence of the polarization effect nor the number of systematic error affecting IP measurements, which can be neglected in ERT surveys. Hence, in this work, we investigate the possible contributions of single-frequency IP and SIP imaging methods to the non-invasive geophysical investigation of landslides. We present imaging results for data collected at the La Valette landslide located in the French Alps, where numerous studies have been conducted and detailed information on the subsurface conditions of the landslide is available.

In order to set the basis for future IP and SIP surveys on landslides, we test different parameters for data collection, especially the electrode configuration, and discuss the particular sources of systematic errors in SIP measurements. With the same objective, we provide sufficient details on the data processing and the quantification of data error.

2. Material and methods

2.1. The time- and frequency-domain IP methods

The IP method is based on four-electrode measurements, where two electrodes are used to inject a current (I) into the ground and the two other electrodes measure the resulting voltages (V). IP measurements can be performed in either time domain (TDIP) or frequency domain (FDIP). TDIP data are commonly expressed in terms of the measured resistance (R), which is the voltage-to-current ratio (V/I), and the integral chargeability, which measures the magnitude of the secondary voltage observed after switching the current off. The measured resistance R largely depends on the geometric arrangement of the four-electrode measurement (i.e. the distances between the four electrodes). Knowing the geometric arrangement, each measured R can be converted to the so-called apparent resistivity (ρ_{app}), which is the electrical resistivity of an equivalent homogeneous half space.

In FDIP, current injections are performed with alternating current, and the measurements are usually given in terms of the measured resistance (R) and an apparent phase shift (ϕ_{app}) between current and voltage. FDIP measurements repeated at different frequencies of the injected current (typically < 1 kHz) are commonly referred to as spectral induced polarization (SIP) and provide information about the frequency dependence of the electrical properties.

Inversion results of FDIP and SIP data are commonly given in terms of the complex conductivity (σ^*). Detailed reviews of IP methods can be found in Sumner (1976), Ward (1988), and Kemna et al. (2012), amongst others.

2.2. The complex conductivity (σ^*)

The electrical properties of the subsurface materials in the low-frequency range (below ~100 kHz) can be represented by the complex conductivity, CC (σ^*), or its inverse, the complex resistivity (ρ^*). The CC consists of a real (σ') and an imaginary (σ'') component, which represent the conductive (loss) and capacitive (storage) electrical properties of subsurface materials, respectively. Alternatively, the σ^* can be expressed in terms of its magnitude ($|\sigma|$) and phase (ϕ):

$$1/\rho^* = \sigma^* = \sigma' + i\sigma'' = |\sigma|\, e^{i\phi} \quad (1)$$

where $i = \sqrt{-1}$. In most practical applications, measured phase shifts are sufficiently small (< 100 mrad) to assume that $\sigma' \approx |\sigma|$ and to approximate the phase ϕ with the ratio between real and imaginary component, i.e. $\phi \approx \sigma''/\sigma'$.

The low-frequency CC of subsurface materials is controlled by three main mechanisms (Ward, 1988): (a) matrix conduction through the solid phase, which is important only if a high metal content allows electronic conduction; (b) ionic or electrolytic conduction through the fluid-filled pore space; and (c) surface conduction through the EDL covering the fluid-grain interface.

Due to its high surface area and cation exchange capacity, clay minerals are related to a high contribution of surface conduction, which usually dominates the electric response of clay-rich materials (Waxman and Smits, 1968; Slater and Lesmes, 2002; Revil and Glover, 1998). Hence, the interpretation of electrical images of clay-rich landslides needs to take into account the contribution of surface conductivity, as the electrical response is not only controlled by the conduction through the pore water. Moreover, typical materials involved in landslide processes do not contain significant concentrations of metallic minerals, such that the contribution of matrix conduction may be neglected. Thus, the measured CC can be understood in terms of two mechanisms: electrolytic (σ_{el}) and surface conduction (σ_{surf}). Taking into account the frequency dependence of the surface conduction, the CC can be written as:

$$\sigma^*(\omega) = \sigma_{el} + \sigma^*_{surf}(\omega) \quad (2)$$

where ω is the angular frequency. As noted in Eq. (2), in the low-frequency range, in which the SIP measurements are conducted, σ_{el} shows a negligible frequency dependence, which is not the case of σ_{surf}^*. Rewriting σ_{el} using Archie's model (Archie, 1942) and σ_{surf}^* in terms of its real and imaginary components, the CC can be expressed as (Lesmes and Frye, 2001):

$$\sigma^*(\omega) = [\Theta^m S^n \sigma_w + \sigma'_{surf}(\omega)] + i\sigma''_{surf}(\omega) \quad (3)$$

where Θ represents the porosity, S the saturation, m and n are empirical

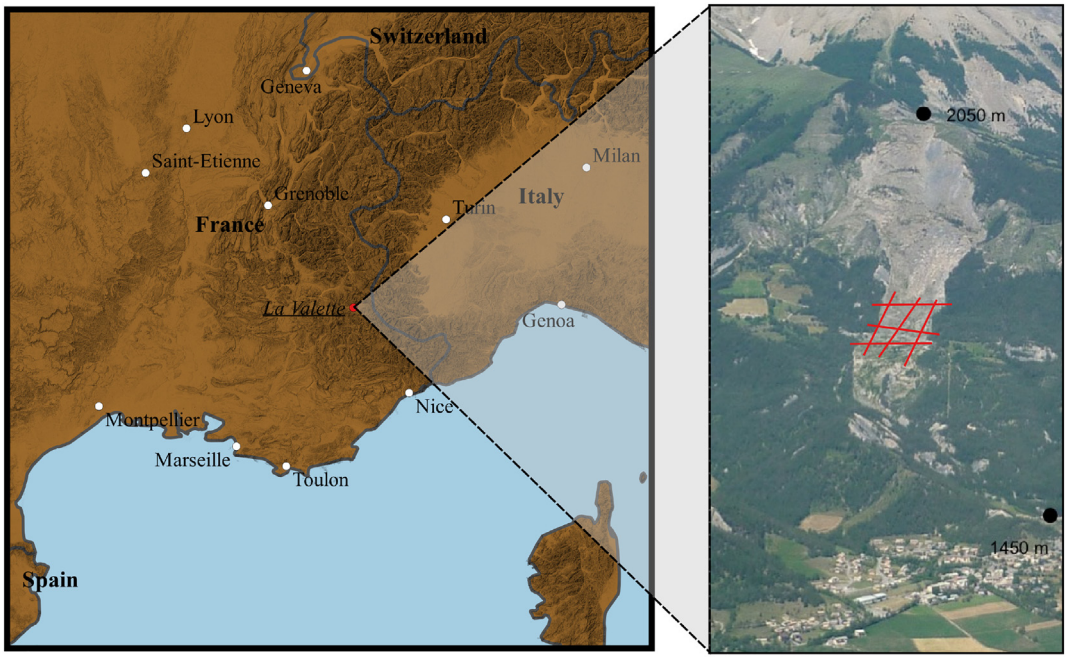

Fig. 1. The La Valette landslide, with its location depicted by the red marker (left) and a picture of the landslide (right) indicating the height (above sea level) of its highest and lowest topographic features. (For interpretation of the references to colour in this figure legend, the reader is referred to the web version of this article.)

coefficients, and σ_w the conductivity of the pore fluid. Eq. (3) shows that the conductivity magnitude $|\sigma|$, as for instance obtained from ERT, is affected by all three components; whereas the imaginary conductivity σ'' assessed by IP measurements only depends on the imaginary part of the surface conductivity. This explains the huge potential of the IP method for an improved lithological characterization of clay-rich landslides.

2.3. The La Valette landslide (South East French Alps)

The La Valette landslide is located in the South East French Alps (Fig. 1), where the presence of a thrust fault separating highly susceptible clay-shale sediments (Jurassic black marls) at the bottom and sandstone and limestone competent rocks at the top is responsible for many landslides in the region (Samyn et al., 2012; Travelletti et al., 2013). The landslide has been triggered in March 1982 at the contact between these two main geological units. The deformation is attributed to the steep slopes and the increase in pore-fluid pressure resulting from the different hydraulic conductivities of the two geological units (Samyn et al., 2012).

The landslide has been subject to numerous investigations using a variety of direct and indirect methods, such as remote sensing (terrestrial and airborne LiDAR), geotechnical analysis of samples recovered from boreholes, and geodetic measurements (e.g., extensometers, inclinometers, GPS), for the spatio-temporal assessment of surface deformation (Raucoules et al., 2013; Malet et al., 2013; Travelletti et al., 2013). Moreover, the internal structure of the La Valette landslide has been characterized through a series of ERT and seismic surveys (Travelletti et al., 2009; Samyn et al., 2012; Hibert et al., 2012). Low electrical resistivity (ρ) values and P-wave seismic velocities (v_p) were generally found to be associated with both the sliding mass consisting of mobilized flysch sediments and the underlying black marls. The lowest values ($\rho < 50$ Ωm and $v_p < 1200\ \mathrm{m{\cdot}s^{-1}}$) were observed in the flysch unit, which extends to a maximum depth of 30 m (see Fig. 2), whereas only slightly higher values (ρ between 60 and 150 Ωm and $v_p > 2000\ \mathrm{m{\cdot}s^{-1}}$) are representative of the underlying black marls (Travelletti et al., 2009, 2013; Samyn et al., 2012; Hibert et al., 2012). Furthermore, the combination of direct and geophysical methods permitted to reconstruct the depth and geometry of the bedrock (Samyn et al., 2012) as presented in Fig. 2.

Nevertheless, the relatively weak electrical contrast between the clay-rich sediments of the sliding mass and the stable black marls limits the applicability of ERT results for an improved hydrogeological understanding, i.e. the delineation of clay-rich zones or preferential groundwater flow paths. Moreover, the subsurface high electrical conductivity is controlled by high clay contents in both the flysch and the black marl units (Ghorbani et al., 2009), which limits the potential of ERT for the monitoring of water saturation (Gance et al., 2016).

2.4. IP measuring protocols and inversion algorithms

SIP measurements were conducted in the central part of the landslide, in the vicinity of the existing borehole B3, where lithological information is available (see Fig. 2) for the validation of the imaging results. SIP data were collected along three long profiles (96 electrodes each) oriented parallel to the flanks (along the main direction of the landslide), and three shorter profiles (64 electrodes each) perpendicular to them, as depicted in Fig. 2. The separation between electrodes in all profiles was 5 m to warrant a depth of investigation of at least 50 m. The measuring device was always placed at the center of the profile (i.e., between electrodes 48 and 49 or 32 and 33, respectively) to reduce the maximum cable length.

SIP data were acquired using an eight-channel impedance tomographer DAS-1 (Multi-Phase Technologies) at 12 frequencies: 0.5, 1, 1.5, 2.5, 5, 7.5, 12, 25, 37.5, 75, 112, and 225 Hz. We tested multiple-gradient (MG) and dipole-dipole (DD) protocols to evaluate their performances in terms of acquisition time, spatial resolution, depth of investigation, and Signal-to-Noise ratio (S/N). These two configurations were selected as they permit the collection of multi-channel sequences (i.e., multiple voltage readings for a given current injection), which is not the case with often-used Wenner or Schlumberger configurations. Furthermore, DD protocols help avoiding potential readings with electrodes previously used for current injection. This is an important consideration because the persistent polarization of electrodes, which have been used for current injections, can result in systematic errors in subsequent voltage readings.

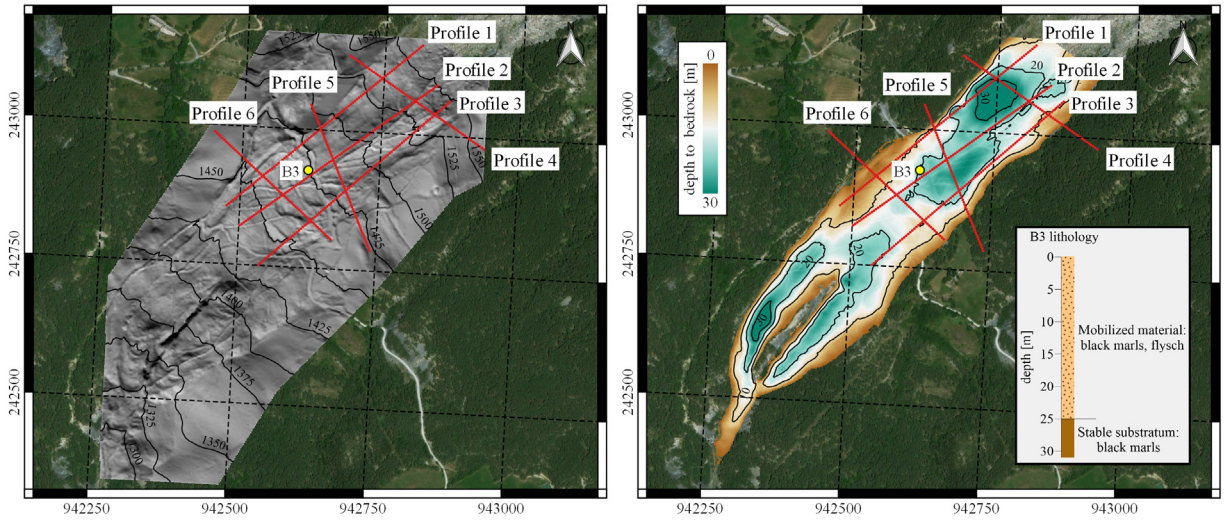

Fig. 2. Location of the SIP profiles at the La Valette landslide (red lines). Left: Terrain relief from an airborne LIDAR-derived digital surface model represented by a hillshade map and elevation contour lines (black lines). The position of the borehole B3 is indicated by the solid circle. Right: Depth to the contact between flysch and black marls (modified from Samyn et al., 2012), with the lithological column of borehole B3 indicated in the inset.

DD data were collected using a constant dipole length, which we define by the number of electrodes "skipped" within a current/potential dipole. For instance, a DD skip-0 denotes measurements with adjacent electrodes. In this study, DD protocols consider measurements to a maximum separation possible between current and potential dipoles. MG protocols were constructed after Dahlin and Zhou (2006), with eight potential dipoles arranged within the current dipole, the length of which increases with the length of the nested potential dipoles (here, skip-0, skip-1, skip-2, and skip-3).

In total, four different measuring protocols were tested: MG, DD skip-0 (DD0), DD skip-3 (DD3) and a combination of skip0 to skip5 (DDmix). Several studies have addressed the comparison of different configurations for the collection of ERT data, while for IP surveys this topic has only been discussed in rare studies (Dahlin and Zhou, 2006). Moreover, previous studies have not addressed the evaluation of the different sources of random and systematic error affecting SIP data. Therefore, our tests consider configurations related to high signal strength (favored by large dipole lengths, such as MG, DD3) and configurations with high spatial resolution (favored by smaller dipole lengths, e.g., DD0).

Inversion algorithms solve for the distribution of electrical properties in the subsurface that explain the measured data. In this study, all datasets were inverted with CRTomo, a smoothness-constraint algorithm by Kemna (2000), which permits the inversion of the data to the confidence level determined by an error model. From a given data set in terms of transfer resistances (R) and apparent phase shifts (ϕ_{app}), the algorithm solves for the distribution of complex resistivity on a 2D grid of lumped finite-element cells. Inversions with CRTomo were performed independently for each frequency. For further details on the inversion procedure, the readers are referred to Kemna (2000).

3. Results and discussion

3.1. Pre-processing of IP datasets

In order to assess the effect on the S/N of the four different measurement configurations, i.e. DD0, DD3, DDmix, and MG, the histograms in Fig. 3 illustrate the distribution of apparent resistivity (ρ_{app}), measured resistance (R), and apparent phase shift (ϕ_{app}) data collected at 1 Hz along Profile 4. In the distributions of ρ_{app}, no significant dependence on the measurement configuration can be observed. This behavior meets the expectations, because for all four configurations, the values of ρ_{app} represent the mean resistivities of comparable volumes of the subsurface, and geometric parameters, such as dipole lengths and the separation between current and potential dipoles, only have a second-order effect. Furthermore, the S/N of the measurement of R (from which ρ_{app} is computed) is high, which prevents the distributions from "smearing out" at the lower and upper limits. The latter effect, however, can be observed in the distribution of ϕ_{app} in the third line of Fig. 3. Especially the DD configurations reveal a large amount of anomalously high and low ϕ_{app} values, which clearly indicates a lower S/N than the one of the MG configuration.

The dependence of the signal strength itself on the measurement configuration can be seen from the distributions of R illustrated in the second line of Fig. 3. The histograms of R reveal variations over three to four orders of magnitude depending on the selected configuration. Moreover, the range of recorded R for the different configurations also changes significantly, with the broadest range related to DD configurations (between 10^{-4} and 1 Ω), evidencing the large dynamic range of recorded voltages (remember that $R \propto V$). Consistently, Fig. 3 exhibits larger variability in ϕ_{app} values for DD measurements, whereas values populate a smaller range for MG measurements.

Although, some authors have proposed to directly analyze voltage readings to assess signal strength, we use the transfer resistances R, which are also sensitive to variations in the injected current I. Besides the measured voltage, I is an important parameter controlling the S/N, which can vary considerably throughout an imaging dataset (e.g., Flores Orozco et al., 2018) depending e.g. on the galvanic contact between electrodes and the ground.

As FDIP measurements are expected to record the response of a chargeable subsurface, the measured resistivity phase shifts should be negative or zero ($\phi_{app} \leq 0$). Thus, positive ϕ_{app} values indicate the presence of random and systematic error in the data. In Fig. 3, particularly DD measurements seem to be affected, whereas the higher S/N reduces the effect of noise on the ϕ_{app} values in MG readings.

However, it is not always indicated to remove all positive ϕ_{app} values: The so-called "negative IP effect" (resulting in positive ϕ_{app} values) has been observed in layered media, where the deepest layer is more conductive than the layer immediately above and the shallowest layer is polarizable (Sumner, 1976). Moreover, negative IP effects have also been reported recently for TDIP (Dahlin and Loke, 2015) under certain geometrical conditions. Although it might be justifiable in some cases, the negative IP effect needs to be treated with caution, as it is the result of systematic errors in most other cases (Flores Orozco et al., 2018). The

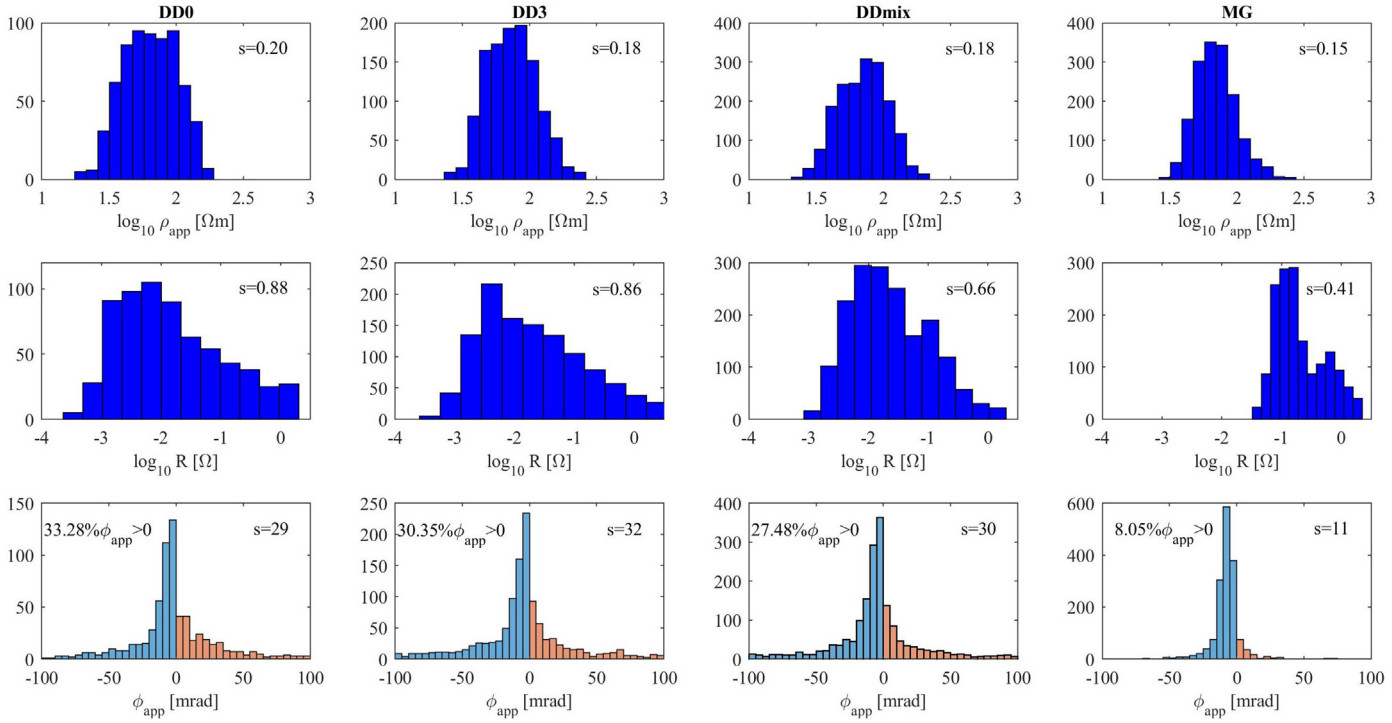

Fig. 3. Histograms of the apparent resistivity ρ_{app} (first line), measured resistance R (second line), and apparent phase shift ϕ_{app} (third line) at 1 Hz along Profile 4 at the La Valette landslide using four different measuring protocols (DD0, DD3, DDmix, and MG). To better assess the variability in the measured values, plots also present the standard deviation (s) computed for each dataset.

latter might be caused by electromagnetic coupling effects, cross talking between wires, poor S/N, or anthropogenic noise (e.g., buried metallic structures) (Dahlin and Leroux, 2012; Flores Orozco et al., 2011, 2012a, 2013; Schmutz et al., 2014; Dahlin and Loke, 2015).

To define the actual range of valid ϕ_{app} readings for the subsequent inversion, it is important to identify outliers in the data. The analysis of the normal and reciprocal misfit (NRM) is a common practice for the characterization of data error in electrical imaging, where reciprocal refer to the re-collection of the normal quadrupole after interchanging the current and potential dipoles. As noted in earlier studies (Labrecque et al., 1996; Slater et al., 2000), the NRM has an important advantage over other methods (e.g., stacking), as it is based on the comparison of two independent measurements and not the repetition of the same reading including the same systematic error. Hence, measurements related to large NRM may indicate those affected by systematic errors, in particular related to poor galvanic contact or problems with the cables (Labrecque et al., 1996). Fig. 4 shows the comparison between normal and reciprocal readings for DD0 measurements along Profile 4. Such plots reveal practically a perfect agreement in transfer resistance for normal (R_n) and reciprocal (R_r) readings. The good agreement of the measurements suggests a negligible level of systematic errors and a minimal distortion due to random errors even for readings with large separations between current and potential dipoles (typically associated with low R values). The apparent robustness of the R measurements also explains the consistency in the ρ_{app} values for measurements with different configurations observed in Fig. 3. Despite of this, Fig. 4 shows large NRM for ϕ_{app} clearly indicating distortions due to systematic and random error.

The NRM of measured resistance (ΔR) and apparent phase shift ($\Delta\phi_{app}$) are analyzed to identify measurements associated with systematic errors or largely dominated by random errors, which need to be removed as outliers prior to the inversion. Here, outliers are defined as those readings related to a NRM exceeding (i) 25% of the value of the corresponding normal or reciprocal; and (ii) two times the standard deviation computed for the entire NRM dataset (~2 mΩ for ΔR and ~5 mrad for $\Delta\phi_{app}$). Before the analysis of NRM, first outliers were defined as those potential readings collected with current injections below 0.001 A, and negative apparent resistivity values, as those readings are clearly related to poor contact between the electrodes and the ground. As observed in the comparison between ϕ_n and ϕ_r (Fig. 4d), following the removal of outliers after the analysis of NRM, it is possible to define maximum and minimum threshold values (here, between ~ 20 and 0 mrad), which can then be used for the identification of outliers in MG measuring schemes lacking reciprocal readings. Pseudo-sections for the data collected along Profile 4 after removal of outliers based on the aforementioned approach are presented in Fig. 5. It is notable that most of the outliers are mainly associated to deep levels with a low S/N.

After the removal of outliers, the remaining measurements are assumed to be affected only by random errors, the magnitude of which can be incorporated into the inversion, by means of error models as proposed by Labrecque et al. (1996), and Slater et al. (2000). These studies recognized a linear increase of the data error of the measured resistance (ΔR) with R (Figure 4c), whereas a negative power-law model (Figure 4f) has recently been adopted to describe $\Delta\phi_{app}$ as a function of R (Flores Orozco et al., 2012a;). As we can see from Fig. 4, these error models also describe the data uncertainty for the measurements collected at La Valette landslide. Hence, error parameters were computed using the bin analysis described in Flores Orozco et al. (2012a).

The advantage of deploying error models, instead of individual errors, is that the same error parameters can be used for the inversion of datasets lacking reciprocal readings, such as MG configurations (e.g., Flores Orozco et al., 2018). Inversions were conducted independently for each dataset collected with different electrode configurations, using the error models defined as $\Delta R = 0.001\Omega + 1.3R$, and $\Delta\phi = 1.19$ mrad $(R/\Omega)^{-0.23}$. The resulting imaging results are presented in Fig. 6, in terms of the real (σ') and imaginary (σ'') components of the complex conductivity. Blanked regions in the electrical images are related to low cumulative sensitivity values (< -3 in the logarithmic normalized value), a parameter that can be used as a proxy for the depth of

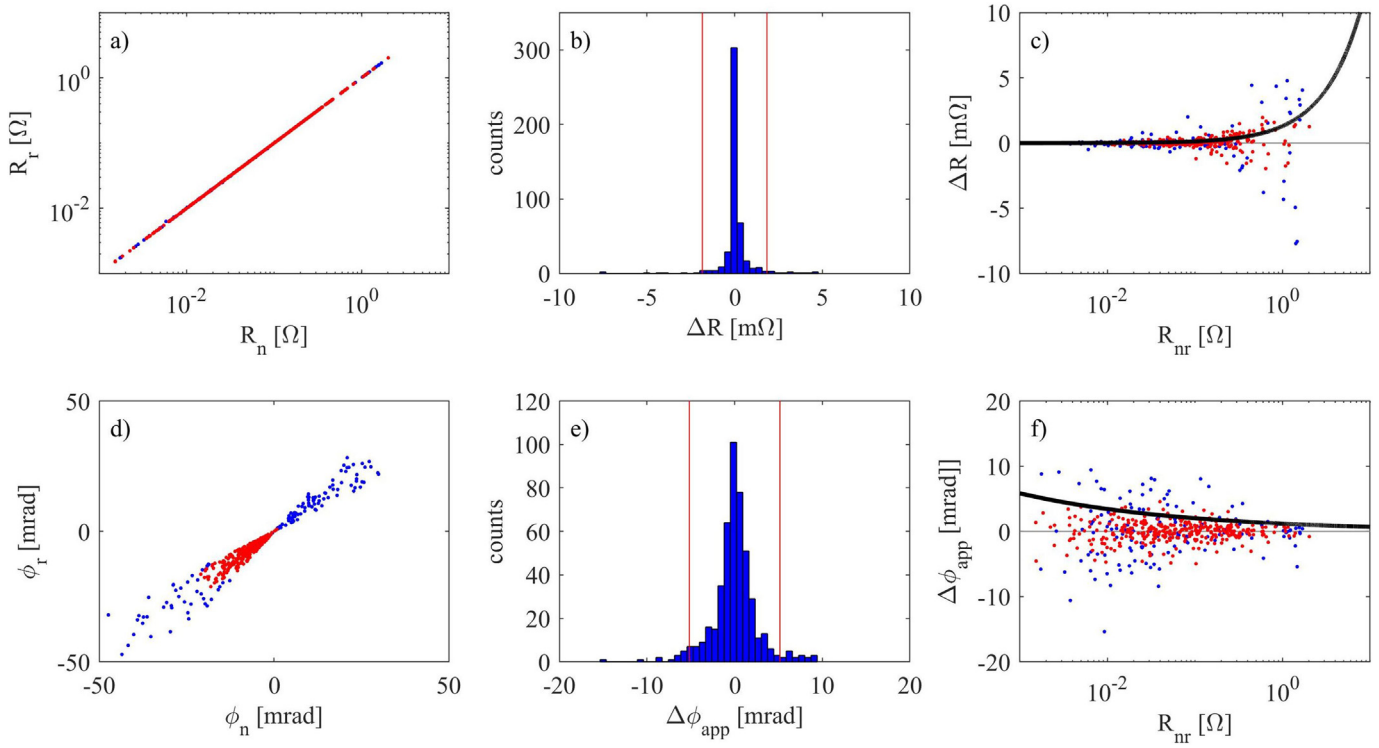

Fig. 4. (a) Comparison between normal and reciprocal readings for transfer resistances R and (d) the apparent phase shifts ϕ_{app}. (b) Histograms of the data error for resistance (ΔR) and (e) apparent phase shift ($\Delta\phi_{app}$) measurements reveal a normal distribution. The values of two standard deviations, which we used as limiting values for the identification of outliers, are indicated by red lines. The dependencies of ΔR (c) and $\Delta\phi_{app}$ (f) on the signal strength R are consistent with previous observations, permitting to define error models (solid black lines). The plots show all readings (blue symbols) and those accepted after removal of outliers (red symbols). (For interpretation of the references to colour in this figure legend, the reader is referred to the web version of this article.)

investigation of IP inversion results (see Weigand et al., 2017, for further details).

3.2. SIP imaging results

Fig. 6 shows SIP imaging results obtained for data collected with DDmix configurations at 0.5, 2.5 and 15 Hz along profiles parallel to the main landslide direction (Profiles 1, 2, and 3). The σ' model is only visualized for the lowest frequency of 0.5 Hz, as the results revealed no changes for data collected at higher frequencies. In general, all sections reveal high electrical conductivities in all subsurface materials, with σ' varying over a narrow range (between 10 and 30 mS/m). These results are consistent with previous investigations at the La Valette landslide (Travelletti et al., 2009; Hibert et al., 2012) and the nearby Super-Sauze landslide (Schmutz et al., 2000) developed in the same lithology. At the same time, the σ'' images, i.e. the polarization effect, reveal a much larger variability with σ'' values ranging between 1 and 800 μS.m^{-1}.

In the case of the real component of the electrical conductivity (σ'), high values correspond to the landslide body, i.e., the mix of weathered blocks of black marls and flysch, indicated by the dashed line in Fig. 6;

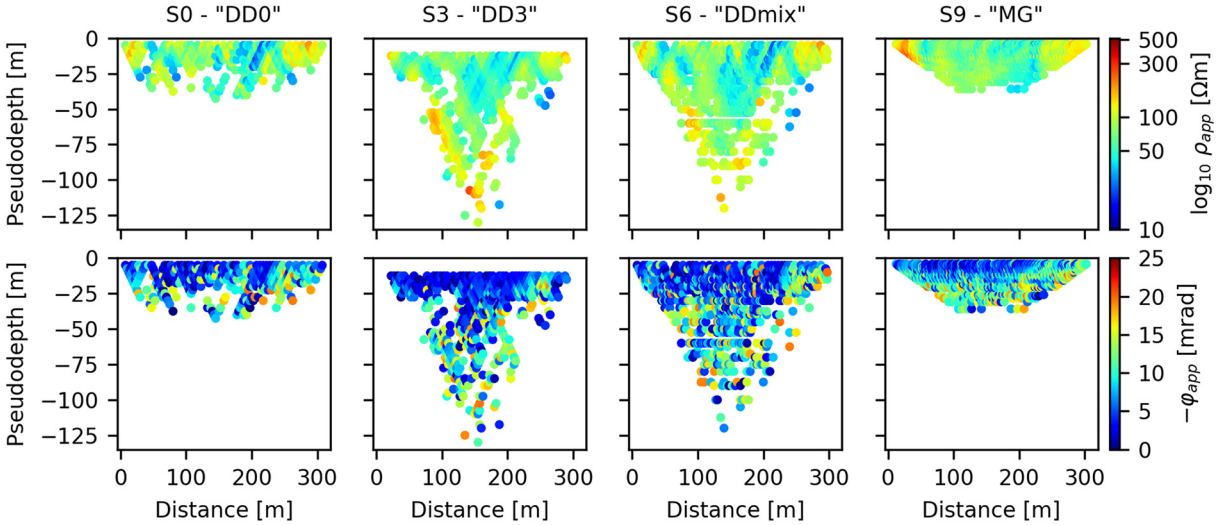

Fig. 5. Raw data measurements presented in pseudo-sections in terms of the apparent resistivity (ρ_{app} - top row) and apparent phase shift (ϕ_{app} – bottom row) for data collected along Profile 4 using DD0, DD3, DDmix, and MG protocols.

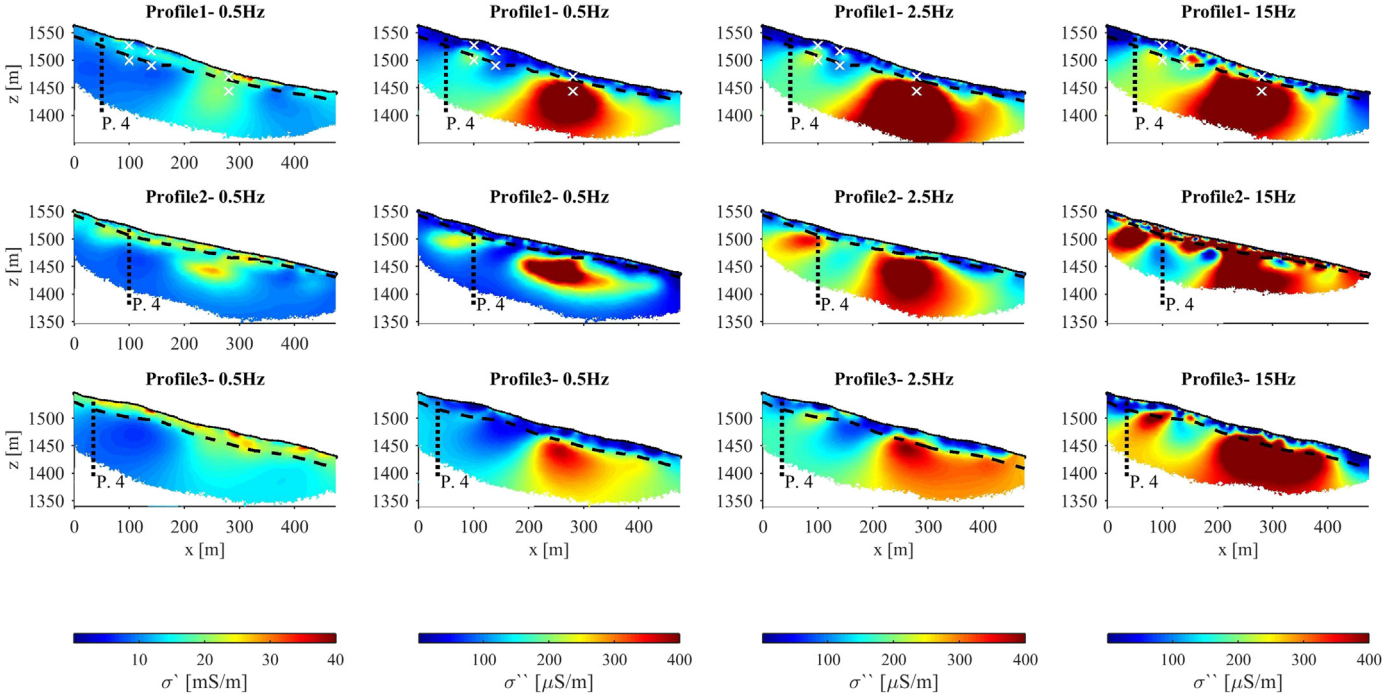

Fig. 6. SIP imaging results obtained from DDmix data collected along Profile 1, 2 and 3 expressed in terms of the real (first column - for data collected at 0.5 Hz) and imaginary components (columns 2 to 4 for data collected at 0.5, 2.5, and 15 Hz) of the CC. Dashed lines parallel to the surface indicate the position of the sliding plane as obtained from wellbore and seismic data (Samyn et al., 2012). The position of the intersection with the perpendicular Profile 4 is indicated by the dashed vertical line. The position of the pixel values extracted for the discussion of the spectral response is indicated by the white symbols (x) along Profile 1.

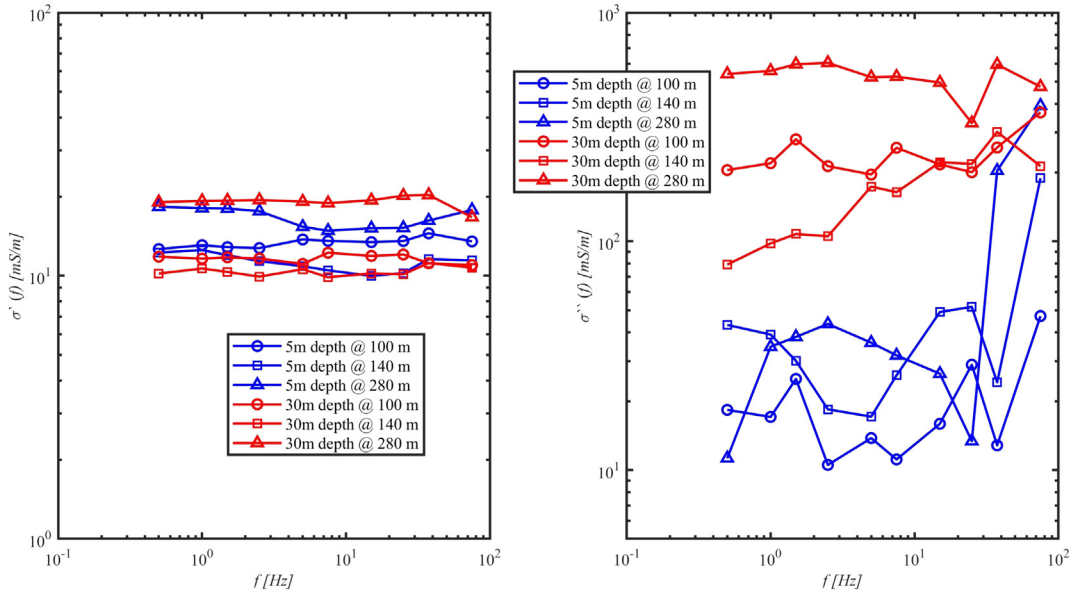

Fig. 7. SIP response for selected pixels retrieved from imaging results obtained for data collected along Profile 1 using the DDmix configuration. The data plotted represent the median of model parameters within a pixel of 4 m radius centered at 100 m (circles), 140 m (squares) and 270 m (triangles), and at depths of 5 m (in blue) and 30 m (in red) associated to the sliding mix of weathered black marls and flysch unit and the underlying black-marl bedrock, respectively. (For interpretation of the references to colour in this figure legend, the reader is referred to the web version of this article.)

lower values ($\sigma' < 10$ mS·m^{-1}) are generally observed within the underlying stable unit, corresponding to the black marls. However, locally, high conductivities also appear well below this lithological contact between the loose materials and the black-marl bedrock (particularly between 200 and 300 m along Profiles 1 and 2) reducing the usefulness of the real component of the CC for the delineation of this geometrical boundary. Similar ambiguities, which make the determination of the landslide body from ERT profiles alone difficult, have been reported before (Travelletti et al., 2009, 2012, 2013; Gance et al., 2016).

As the visualization of the imaginary component of the electrical conductivity (σ'') in Fig. 6 illustrates, this additional property can largely reduce the ambiguity of electrical imaging. Here, the landslide body stands out clearly by a weak polarization response ($\sigma'' < 100$ μS.m^{-1}), whereas the underlying black marls are generally more polarizable. Particularly, the conductive anomalies below the sliding

plane (dashed lines), which make the σ' (or equally ERT) images inconclusive, are associated with the highest polarization responses (σ'' up to 800 μS.m^{-1}) and help to distinguish the conductive landslide body from conductive anomalies within the bedrock unit.

While the amplitude of the polarization effect (σ'') turns out to be particularly helpful to reduce the uncertainty of electrical imaging on the La Valette landslide and aid the delineation of the landslide body, the large variability of σ'' values below the sliding plane raise new questions regarding the electrical response of the underlying unit. Based on information available near the SIP lines (lithological description in sediments recovered at B3), we must assume that the black marls underlie the entire landslide body at an average depth of ~25 m (Travelletti et al., 2009; Samyn et al., 2012). Consequently, we do not expect any lithological changes in the bedrock along the SIP Profiles 1 to 3. Thus, the observed lateral changes in σ'' must be attributed to local variations in the composition, fracturing, and/or weathering of the black marls.

In the absence of sufficiently dense borehole data, a more detailed analysis of the frequency dependence of the CC can further aid the interpretation of the electrical imaging results. Fig. 7 shows the spectral variation (i.e., frequency dependence) of σ' and σ'' at three different positions along Profile 1 and two different depths: (i) the flysch unit at 5 m depth and (ii) the black marls at 30 m depth. The σ' spectra in the left panel reconfirm the aforementioned observation that the real part of the conductivity is not indicative for the two principal lithological units, as the conductivity of the black marl unit varies over a wide range. In addition, they reveal practically no frequency dependence for σ'. Meanwhile, the polarization effect, presented in terms of σ'', reveals different magnitudes and spectral behaviors for the two units. The mix of weathered blocks of black marls and flysch materials exhibit low and practically constant σ'' values at frequencies below 30 Hz, whereas within the more polarizable black-marl unit, the σ'' values are approximately one order of magnitude higher and small peaks can be observed around 1.5–2.5 Hz (at 100 m and 280 m) and at 5–15 Hz (100 m and 140 m). In particular the spectra for pixel values recovered at 140 m (along profile direction) in the black marls reveal a linear increase in σ'' with increasing the frequency, consistent to the observations from Ghorbani et al. (2009), for measurements in the laboratory in black marls samples recovered in the Super-Sauze landslide, which is located in the same lithology as the La Valette landslide.

Imaging results presented in Figure 6 and 7 show the potential of the SIP method for the investigation of landslide architecture. However, the SIP measurements are related to lower S/N than ERT, as well as additional sources of systematic errors. Hence, an adequate processing of SIP data is critical for the inversion of quantitative meaningful electrical models. Hence, in Fig. 8, we present a workflow illustrating the iterative steps for an adequate processing of single-frequency and spectral IP datasets: (1) identification of clear outliers; (2) normal-reciprocal analysis; (3) detailed identification of outliers; (4) quantification of data error; (5) inversion of the dataset; (6) verification of the imaging results through complementary information; and (7) interpretation of subsurface electrical properties.

3.3. Electrical properties of geological units

The amplitude and frequency dependence of both components of the CC (σ' and σ'') in pixels retrieved from the black-marl bedrock are in good agreement with existing laboratory SIP measurements on clay-rock samples. In our field measurements, σ' roughly varies between 10 and 20 mS/m in the intact black marls and exhibits a constant value at the different frequencies here investigated (< 100 Hz). In their analysis of seven clay-rock samples from three different formations, including black marls, Ghorbani et al. (2009) found a slightly larger variability in the σ' values (~5 to 80 mS·m^{-1}) but the same negligible frequency dependence. As written in Eq. (2), the surface conduction contributes to both the real and imaginary components of the CC. Hence, the comparably high electrical conductivities are largely due to the contribution of surface conduction (σ_{surf}' in Eq. (3)) associated to clay minerals. Accordingly, in the study by Ghorbani et al. (2009) the σ' values roughly correlate with the clay content of the investigated samples. For the present data set, this implies that observed changes in σ' below the sliding plane (for instance in spectra presented in Fig. 7) are indicative of variations in the clay fraction in the stratified black marls.

The mobilized flysch of the landslide body tends to be associated with slightly higher electrical conductivity (σ') values. Also in this clay-rich unit, surface conduction is expected to contribute a significant part to the overall conduction. Thus, besides a higher contribution of electrolytic conduction through the porous sediments (compared to the tight black marls), the higher σ' values might be due to a higher clay content of the loose material.

Furthermore, the imaginary part of the conductivity σ'' inferred from our SIP field measurements are in good agreement with the laboratory studies by Ghorbani et al. (2009). While our field measurements resulted in σ'' values between 80 and 600 μS·m^{-1} in the black marls, the laboratory study reports values between 1 and 600 μS/m over a comparable frequency range. The frequency dependencies of field and laboratory data also show a similar behavior. Both the near-linear increase (on a log-log scale) of σ'' observed in the less polarizable zone at 140 m (see Fig. 7) as well as the near-constant behavior with slight peaks observed in the more polarizable zones around 100 m and 280 m can also be found in the laboratory data set. In both data sets, σ'' peaks tend to be associated with higher polarization magnitudes.

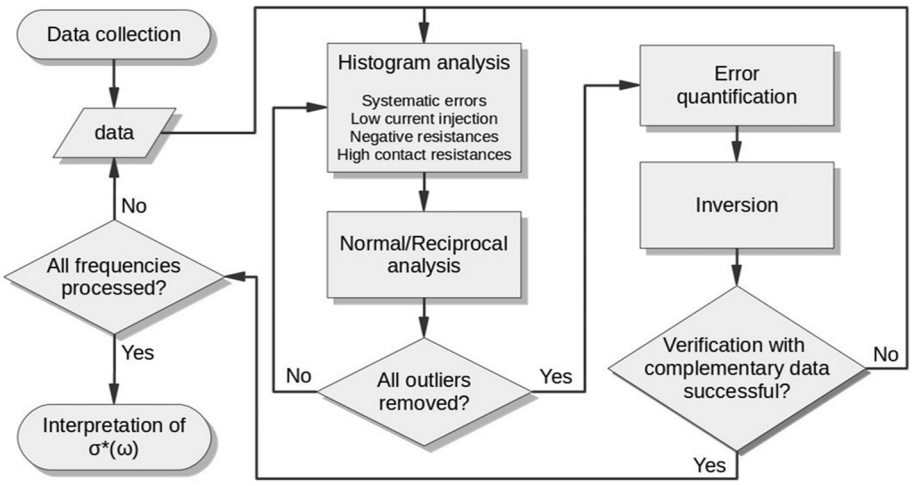

Fig. 8. Workflow chart presenting the iterative processes for the processing of IP and SIP datasets.

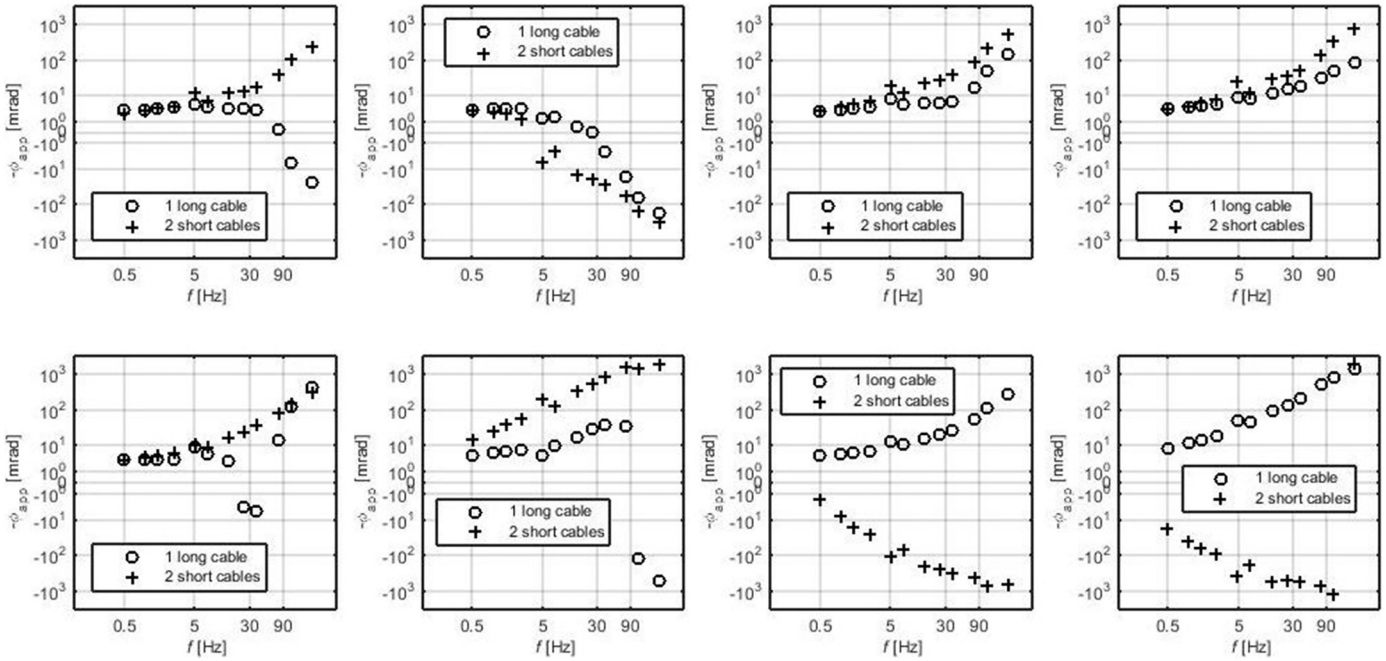

Fig. 9. Representative apparent phase-shift (ϕ_{app}) spectra collected with current and potential dipoles in the same cable bundle (open circles) and using separate cable bundles for current and potential electrodes (crosses). For the measurements in the same cables, current injections were performed between electrodes 1 and 2 and the potential readings where collected by adjacent electrode pairs between electrodes 3 to 11, representing the longest separations from the measuring device. Whereas measurements with separate cables used current injections between electrodes 31 and 32 and potential readings performed with electrodes between 33 and 41 using adjacent electrode pairs, which represent the shorter cable lengths to the measuring device. Measurements refer to the eight potential differences collected with adjacent electrodes (DD0 protocol) for a given current injection.

Changes in the shape of the σ'' spectra are, consistently to Ghorbani et al. (2009), based on variations in the clay content and the chemical composition of the clay minerals.

The spectral position of the polarization (σ'') maximum is generally attributed to a characteristic grain size (e.g., Revil and Florsch, 2010) or a characteristic pore size (e.g., Binley et al., 2005). The low-frequency (i.e. 1.5–2.5 Hz) polarization maximum observed in the black marls points to a slow polarization processes dominated by large grains (or pores). As Ghorbani et al. (2009) argue, relatively large non-clayey (i.e. quartz and calcite) grains surrounded by much smaller clay minerals are the most probable reason for the slow polarization process.

The lack of a clear polarization maximum and the smaller polarization magnitude in the mix of weathered black marls and flysch unit indicates a homogeneous distribution of large non-clay grains, with the increase in σ'' at high frequencies (> 10 Hz) likely indicating a fast polarization resulting from disperse (i.e. not attached to the larger grains) fine grains in flysch materials. Moreover, plots in Fig. 7 reveal an erratic behavior at higher frequencies (> 30 Hz) in the black marls and a steep increase of σ'' in the flysch sediments. This high-frequency response in SIP measurements is generally related to the occurrence of electromagnetic coupling in the data.

3.4. Electromagnetic coupling in SIP imaging data

The critical frequency (f_c) refers to the frequency at which the polarization response has a maximum (i.e., peak), and, as mentioned before, is attributed to a length scale (grain or pore size), which is also controlling groundwater flow (Binley et al., 2005; Slater, 2006). Hence, petrophysical relationships linking hydrogeological and electrical parameters are based on the relaxation time (Revil and Florsch, 2010), which is inversely proportional to f_c. However, SIP field measurements performed at relatively high frequencies (> 25 Hz) are often affected by distortions due to electromagnetic (EM) coupling, impeding a quantitative determination of relaxation times at high frequencies.

In SIP data, EM coupling is known to be an important source of systematic error, in particular at high frequencies. However, some studies have shown that even at relatively low frequencies (around 4 Hz), EM distortions can affect ϕ_{app} readings (Flores Orozco et al., 2011). EM coupling may occur due to (i) inductive effects taking place in conductive subsurface materials due to current flowing during current injections (Schmutz et al., 2014); (ii) mutual impedances between the wires connecting the potential and the current dipoles (Zimmermann et al., 2008, and references therein); and (iii) capacitive effects due to parasitic EM fields resulting from differences in the contact impedances between the electrodes and the subsurface or between the conductive shield of the cable and the surface (Zhao et al., 2013).

EM (inductive) coupling is proportional to the conductivity of the ground, the frequency and the squared cable length connecting the electrodes (Hallof, 1974). Consequently, it can be expected to affect high-frequency IP measurements (> 1 Hz), in particular in clay-rich materials related to high σ', as observed at the La Valette landslide. Over the last decades, several studies have proposed to use numerical modeling of the high-frequency EM response of homogeneous and layered conductive media to remove the effect of EM coupling from different dipole configurations (Hallof, 1974; Routh and Oldenburg, 2001). However, rough topographies, such as the one of the La Valette landslide, significantly influence the geometry of the cables and put a limit to such EM decoupling approaches. Moreover, such corrections do not address capacitive coupling.

A different approach fits a Cole-Cole relaxation model to the high-frequency response and subtracts this response from the measured values (Pelton et al., 1978). Kemna (2000) demonstrated the applicability of such approach in tomographic applications and extended the method to account for positive and negative EM effects, which reflect dominating inductive or capacitive coupling. Meanwhile, other authors have investigated field methodologies to avoid, or minimize, EM coupling, such as the deployment of separate cables for current injections and potential measurements (Dahlin et al., 2002; Dahlin and Leroux, 2012).

To assess EM coupling in our SIP measurements and illustrate some practical limitations of the aforementioned decoupling approaches, Fig. 9 shows representative DD0 apparent phase spectra for eight potential dipoles. SIP measurements were collected using two different setups: (a) current injection between electrodes 1 and 2 and potential readings between adjacent electrode pairs between electrodes 3 to 10, to illustrate the effect of EM coupling due to one long multi-core cable (160 m length); and (b) current injection between electrodes 31 and 32 and potential readings between adjacent electrode pairs between electrodes 33 to 41 using two short (10 m) and separate cables, one for current injection and the other for potential dipoles. Although the geometries of the measurements vary significantly, all apparent phase spectra in Fig. 9 reveal similar trends at high frequencies: a linear increase (or decrease) of ϕ_{app} with frequency, which sets on at about 25 Hz and is clearly indicative of EM coupling.

The spectra in Fig. 9 demonstrate that even separating current from potential cables does not yield a significant improvement of high-frequency measurements. Most likely, either capacitive coupling or induction in the conductive subsurface dominates over cable effects. Furthermore, EM coupling may result in sign reversals, which can be attributed to dominating inductive (commonly negative ϕ_{app} values) or capacitive (commonly positive ϕ_{app} values) effects. Although not discussed here, the recollection of measurements after splitting dipoles for current injection and potential readings in separate cables (Dahlin and Leroux, 2012) may help to distinguish which IP readings are still within the range of negligible EM coupling.

Application of the decoupling method proposed by Pelton et al. (1978) resulted in corrected ϕ_{app} values below 1 mrad (data not shown). This clearly indicated that the readings were dominated by EM coupling and no information about the subsurface polarization response could be recovered from high-frequency (above 25 Hz) readings.

The deployment of instruments using fiber optic instead of ERT multicore cables has also been proposed to improve the collection of IP data at high frequencies (Schmutz et al., 2014). However, previous studies deploying such instruments also revealed EM coupling in the data starting at ~30 Hz (Flores Orozco et al., 2012b). Alternatively, the use of coaxial cables demonstrated the possibility to collect SIP data without apparent EM coupling over the frequency range between 0.06 and 100 Hz (Flores Orozco et al., 2013), maybe offering a possibility for further research in the investigation of clay-rich landslides.

The collection of data with potential electrodes placed within the current dipole (MG, Wenner or Schlumberger arrays) is also related to strong EM coupling in SIP datasets (Flores Orozco et al., 2013). Furthermore, such configurations bear the risk of contamination of the apparent phase readings due to polarization of the electrodes placed within the current pathways. Hence, DD configurations are commonly recommended for the collection of both single frequency IP and SIP measurements.

3.5. IP imaging results for different electrode configurations

To evaluate possible effects of the electrode configuration on the SIP imaging results, Fig. 10 shows CC images obtained from data at 1 Hz collected along Profile 4 using different electrode configurations, DD0, DD3, DDmix, and MG. All datasets were pre-processed following the procedure presented in the section Pre-processing of IP data sets described above.

In general, the images of the real component of CC (σ', first column in Fig. 10) show consistent results for measurements collected with different measuring protocols. Yet, it is noticeable that the DD0 protocol has the lowest depth of investigation ($\leq$50 m, as indicated by the blanked-out areas), whereas DD3, DDmix and MG configurations yield similar depths of investigation of about 70 m and deeper. The low depth of investigation of the DD0 configuration is expected and can be explained by the reduced maximum separation between current and potential dipoles. Nevertheless, all configurations are sensitive down to depths well below the sliding plane located between 5 and 30 m below ground surface (see dashed line in Fig. 10). Regarding the main units resolved in the σ' images presented in Fig. 10, results are consistent with those along Profile 2 (see Fig. 6), where the flysch unit stands out with high electrical conductivity values and the stable black marls exhibit slightly lower σ'.

Images of the polarization effect (σ'', second column in Fig. 10) also show structures, which are consistent with those observed along Profile 2 (see Fig. 6). Maximum σ'' values along Profile 4 do not exceed ~200 μS/m, which are in agreement with maximum σ'' values in the upper part of Profile 2, where the two profiles intersect. Again, the flysch unit above the sliding plane is found to have a low polarization response ($\sigma'' < 100\ \mu S \cdot m^{-1}$), whereas higher polarization responses ($\sigma'' \sim 200\ \mu S \cdot m^{-1}$) can be found right below the contact between the mix of weathered black marls and flysch unit and the intact black-marl bedrock.

Regarding the spatial resolution of the different σ'' anomalies, Fig. 10 reveals differences between the four measurement configurations. Sharp contacts of the polarizable anomalies, especially those located between ~100 and ~200 m, indicate a higher spatial resolution of the three DD configurations as compared to the MG configuration. Furthermore, the four different measurement configurations resolve different polarizable anomalies. The DD0 results reveal polarizable anomalies only in the vicinity of the sliding plane; whereas DD3, DDmix and MG configurations resolve deeper anomalies, which are located below the sliding plane and extend beyond the limits of the sliding mass deep into the black marls forming the left and right flank (anomaly between ~200 and ~300 m). These deep anomalies are most pronounced in the images obtained from the MG data, which might be related to the high S/N of this configuration (c.f., Fig. 3). Performing the inversion with error parameters determined from the normal-reciprocal misfit of the DD configurations (associated to lower S/N) may over-estimate data error in MG measurements, which are associated to much larger transfer resistance values than those in DD measurements as observed in Fig. 3; thus resulting in a slight over-fitting in MG images, leading to the creation of the high polarizable anomaly values observed in Fig. 10.

Conclusively, the DDmix measuring protocol presents a good trade-off between spatial resolution and S/N. Furthermore, as mentioned before, DD measuring protocols can be designed to avoid the collection of voltage readings with electrodes previously used for current injection. An adequate processing of the raw data (see section Pre-processing of IP data sets) permits the computation of consistent imaging results independently of the selected measuring protocol. Furthermore, nested potential dipoles within the current dipole may enhance electromagnetic coupling in the data.

4. Conclusions

We present the application of single-frequency IP and SIP imaging results for the understanding of hydrogeological units at the La Valette landslide. We demonstrate that a careful processing of the IP data regarding (1) the detection and removal of outliers and (2) the quantification of random error permits to solve for consistent imaging results obtained along different profiles, and independently of the deployed electrode configuration. We also demonstrate the distortion in the SIP measurements due to EM coupling, a topic rarely addressed in field IP application but that may largely affect the interpretation of the electrical images. Our data reveal EM coupling even at the low frequencies, starting at ~25 Hz, even for data collected using separate cables for current injections and potential measurements.

Our results demonstrate the possibility to improve the interpretation of electrical conductivity images in clay-rich landslides by adding the information gained by means of the images of the polarization effect. Results presented here revealed two main units: a conductive and low polarizable unit corresponding to the sliding mix of black marls and

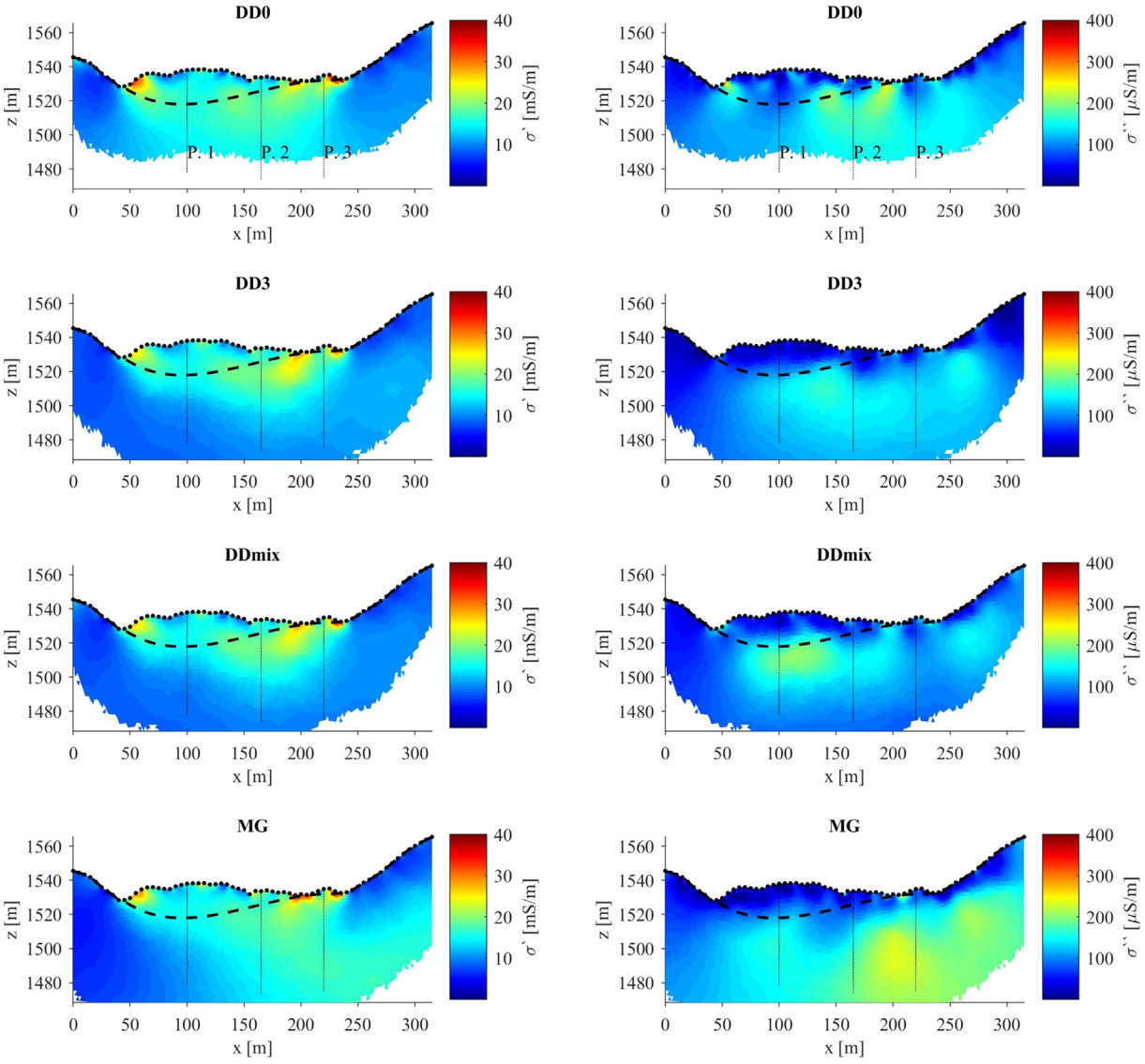

Fig. 10. CC imaging results for data collected along Profile 4 using different electrode configurations, expressed in terms of the real (left row) and imaginary (right row) component of the CC. Dashed horizontal lines indicate the position of the sliding plane as obtained from wellbore and seismic data (Samyn et al., 2012). Vertical lines indicate the intersections with Profiles 1, 2, and 3 (from left to right).

flysch materials on top of slightly less conductive black-marl bedrock, which is correlated to an enhanced polarization response. Imaging results of the polarization effect help to better delineate the contact between the two units, as well as lateral variations in the black marls, which may be indicative of variable hydraulic properties. The contact between materials with different hydraulic properties is commonly associated to zones vulnerable to landslides due to the undesired increase in pore-fluid pressure following rainfall events. Hence, the lateral changes observed in the black marls through the SIP images are likely indicative of changes in the clay fractions and the corresponding variations in hydraulic conductivity. It is also worth noting here that seismic surveys would also fail to identify the anomaly revealed in the SIP images, considering that the mechanical properties of flysch and alluvial sediments are similar. Furthermore, the interpretation of solely resistivity properties gained by means of ERT is limited, as observed in σ' plots in Fig. 6.

Our results suggest that SIP imaging is a suitable method to improve the understanding of landslides, in particular, to improve the interpretation of electrical conductive materials such as clay-rich geological media. Nevertheless, further investigations at La Valette landslide are required to fully validate the interpretation of the SIP imaging results presented here. We believe that SIP imaging results could be used to help designing the collection of soil and water sampling campaigns to fully understand the electrical, hydraulic and geotechnical properties of the subsurface.

Acknowledgments

The preparation of this material is supported through the Austrian Science Fund (FWF) – Agence Nationale de la Recherche (ANR) research project FWF-I-2619-N29 and ANR-15-CE04-0009-01 HYDROSLIDE: *Hydro-geophysical observations for an advanced understanding of clayey landslides*. We also want to thank Veronika Rieckh, Martine Trautmann, Kusnahadi Susanto, Eric Stell, and Colas Bohy for their help during the fieldwork. We also want to thank the Editor, the Guest Editor Michel Jaboyedoff and three anopnymous reviewers for their comments and suggestions that significantly improved the quality of this manuscript.

References

Archie, G.E., 1942. The electrical resistivity log as an aid in determining some reservoir

characteristics. Trans. AIME 146 (1), 54–62.
Binley, A., Slater, L.D., Fukes, M., Cassiani, G., 2005. Relationship between spectral induced polarization and hydraulic properties of saturated and unsaturated sandstone. Water Resour. Res. 41, W12417.
Binley, A., Hubbard, S.S., Huisman, J.A., Revil, A., Robinson, D.A., Singha, K., Slater, L.D., 2015. The emergence of hydrogeophysics for improved understanding of subsurface processes over multiple scales. Water Resour. Res. 51 (6), 3837–3866.
Brückl, E., Brunner, F.K., Lang, E., Mertl, S., Müller, M., Stary, U., 2013. The Gradenbach observatory—monitoring deep-seated gravitational slope deformation by geodetic, hydrological, and seismological methods. Landslides 10, 815–829.
Bücker, M., Hördt, A., 2013. Long and short narrow pore models for membrane polarization. Geophysics 78 (6), E299–E314.
Dahlin, T., Leroux, V., 2012. Improvement in time-domain induced polarization data quality with multi-electrode systems by separating current and potential cables: near surface. Geophysics 10 (6), 545–565.
Dahlin, T., Loke, M.H., 2015. Negative apparent chargeability in time-domain induced polarisation data. J. Appl. Geophys. 123, 322–332.
Dahlin, T., Zhou, B., 2006. Multiple-gradient array measurements for multichannel 2D resistivity imaging: near surface. Geophysics 4 (2), 113–123.
Dahlin, T., Leroux, V., Nissen, J., 2002. Measuring techniques in induced polarisation imaging. J. Appl. Geophys. 50 (3), 279–298.
Flores Orozco, A., Williams, K.H., Long, P.E., Hubbard, S.S., Kemna, A., 2011. Using complex resistivity imaging to infer biogeochemical processes associated with bioremediation of an uranium-contaminated aquifer. J. Geophys. Res. 116 (G3), 2156–2206 Biogeosciences.
Flores Orozco, A., Kemna, A., Zimmermann, E., 2012a. Data error quantification in spectral induced polarization imaging. Geophysics 77 (3), E227–E237.
Flores Orozco, A., Kemna, A., Oberdörster, C., Zschornack, L., Leven, C., Dietrich, P., Weiss, H., 2012b. Delineation of subsurface hydrocarbon contamination at a former hydrogenation plant using spectral induced polarization imaging. Journal of Contaminated Hydrology 136-137, 131–144.
Flores Orozco, A., Williams, K.H., Kemna, A., 2013. Time-lapse spectral induced polarization imaging of stimulated uranium bioremediation: near surface. Geophysics 11 (5), 531–544.
Flores Orozco, A., Velimirovic, M., Tosco, T., Kemna, A., Sapion, H., Klaas, N., Sethi, R., Leen, B., 2015. Monitoring the injection of microscale zero-valent iron particles for groundwater remediation by means of complex electrical conductivity imaging. Environ. Sci. Technol. 49 (9), 5593–5600.
Flores Orozco, A., Gallistl, J., Bücker, M., Williams, K., 2018. Decay-curve analysis for data error quantification in time-domain induced polarization imaging. Geophysics 83 (2), E75–E86.
Friedel, S., Thielen, A., Springman, S.M., 2006. Investigation of a slope endangered by rainfall-induced landslides using 3D resistivity tomography and geotechnical testing. J. Appl. Geophys. 60 (2006), 100–114.
Gance, J., Grandjean, G., Samyn, K., Malet, J.-P., 2012. Quasi-Newton inversion of seismic first arrivals using source finite bandwidth assumption: application to subsurface characterization of landslides. J. Appl. Geophys. 87, 94–106.
Gance, J., Malet, J.-P., Supper, R., Sailhac, P., Ottowitz, D., Jochum, B., 2016. Permanent electrical resistivity measurements for monitoring water circulation in clayey landslides. J. Appl. Geophys. 126, 98–115.
Ghorbani, A., Cosenza, P., Revil, A., Zamora, M., Schmutz, M., Florsch, N., Jougnot, D., 2009. Non-invasive monitoring of water content and textural changes in clay-rocks using spectral induced polarization: a laboratory investigation. Appl. Clay Sci. 43 (3), 493–502.
Hallof, P.G., 1974. The IP phase measurement and inductive coupling. Geophysics 39 (5), 650–665.
Hibert, C., Grandjean, G., Bitri, A., Travelletti, J., Malet, J.-P., 2012. Characterizing landslides through geophysical data fusion: example of the La Valette landslide (France). Eng. Geol. 128, 23–29.
Kemna, A., 2000. Tomographic Inversion of Complex Resistivity: Theory and Application. Der Andere Verlag, Osnabrück.
Kemna, A., Binley, A., Cassiani, G., Niederleithinger, E., Revil, A., Slater, L., Williams, K.H., Flores Orozco, A., Haegel, F.H., Hördt, A., Kruschwitz, S., Leroux, V., Titov, K., Zimmermann, E., 2012. An overview of the spectral induced polarization method for near-surface applications: near surface. Geophysics 10 (6), 453–468.
Labrecque, D.J., Miletto, M., Daily, W., Ramirez, A., Owen, E., 1996. The effects of noise on Occam's inversion of resistivity tomography data. Geophysics 61, 538–548.
Lesmes, D.P., Frye, K.M., 2001. Influence of pore fluid chemistry on the complex conductivity and induced polarization responses of Berea sandstone. J. Geophys. Res. Solid Earth 106 (B3), 4079–4090.
Malet, J.-P., Durand, Y., Remaître, A., Maquaire, O., Etchevers, P., Guyomarch', G., Déqué, M., van Beek, L.P.H., 2007. Assessing the influence of climate change on the activity of landslides in the Ubaye Valley. In: McInnes, R., Jakeways, J., Fairbank, H., Mathie, E. (Eds.), Proceedings International Conference on Landslides and Climate Change – Challenges and Solutions. Taylor & Francis, London, pp. 195–205.
Malet, J.-P., Ulrich, P., Déprez, A., Masson, F., Lissak, C., Maquaire, O., 2013. Continuous Monitoring and Near-Real Time Processing of GPS Observations for Landslide Analysis: A Methodological Framework. In: Margottini, C., Canuti, P., Sassa, K. (Eds.), Landslide Science and Practice. Springer, Berlin, Heidelberg.
Maraun, D., Wetterhall, F., Ireson, A.M., Chandler, R.E., Kendon, E.J., Widmann, M., Brienen, S., Rust, H.W., Sauter, T., Themeßl, M., Venema, V.K.C., Chun, K.P., Goodes, C.M., Jones, R.G., Onof, C., Vrac, M., Thiele-Eich, I., 2010. Precipitation downscaling under climate change: Recent developments to bridge the gap between dynamical models and the end user. Rev. Geophys. 48 (3), RG3003.
Marescot, L., Monnet, R., Chapellier, D., 2008. Resistivity and induced polarization surveys for slope instability studies in the Swiss Alps. Eng. Geol. 98 (1), 18–28.
Pelton, W.H., Ward, S.H., Hallof, P.G., Sill, W.R., Nelson, P.H., 1978. Mineral discrimination and removal of inductive coupling with multifrequency IP. Geophysics 43 (3), 588–609.
Raucoules, D., Michele, M., Malet, J.P., Ulrich, P., 2013. Time-variable 3D ground displacements from High-Resolution Synthetic Aperture Radar (SAR). Application to La Valette landslide (South French Alps). Remote Sens. Environ. 139, 198–204.
Revil, A., Florsch, N., 2010. Determination of permeability from spectral induced polarization in granular media. Geophys. J. Int. 181 (3), 1480–1498.
Revil, A., Glover, P.W.J., 1998. Nature of surface electrical conductivity in natural sands, sandstones, and clays. Geophys. Res. Lett. 25 (5), 691–694.
Routh, P.S., Oldenburg, D.W., 2001. Electromagnetic coupling in frequency-domain induced polarization data: a method for removal. Geophys. J. Int. 145, 59–76.
Samyn, K., Travelletti, J., Bitri, A., Grandjean, G., Malet, J.-P., 2012. Characterization of a landslide geometry using 3D seismic refraction traveltime tomography: the La Valette landslide case history. J. Appl. Geophys. 86, 120–132.
Sastry, R.G., Mondal, S.K., 2012. Geophysical characterization of the Salna Sinking Zone, Garhwal Himalaya, India. Surv. Geophys. 1–31.
Schmutz, M., Albouy, Y., Guérin, R., Maquaire, O., Vassal, J., Schott, J.J., Descloîtres, M., 2000. Joint electrical and time domain electromagnetism (TDEM) data inversion applied to the Super Sauze earthflow (France). Surv. Geophys. 21 (4), 371–390.
Schmutz, M., Ghorbani, A., Vaudelet, P., Blondel, A., 2014. Cable arrangement to reduce electromagnetic coupling effects in spectral-induced polarization studies. Geophysics 79 (2), A1–A5.
Slater, L., 2006. Near surface electrical characterization of hydraulic conductivity: from petrophysical properties to aquifer geometries – a review. In: 18th IAGA WG 1.2 Workshop on Electromagnetic Induction in the Earth. El Vendrell, Spain (September 17-23, 2006).
Slater, L., Lesmes, D., 2002. IP interpretation in environmental investigations. Geophysics 67 (1), 77–88.
Slater, L., Binley, A., Daily, W., Johnson, R., 2000. Cross-hole electrical imaging of a controlled saline tracer injection. J. Appl. Geophys. 44, 85–102.
Sumner, J.S., 1976. Principles of Induced Polarization for Geophysical Exploration. Elsevier, Amsterdam.
Supper, R., Ottowitz, D., Jochum, B., Roemer, A., Pfeiler, S., Kauer, S., Keuschnig, M., Ita, A., 2014. Geoelectrical monitoring of frozen ground and permafrost in alpine areas: field studies and considerations towards an improved measuring technology: near surface. Geophysics 12 (1), 93–115.
Travelletti, J., Malet, J.-P., Hibert, C., Grandjean, G., 2009. Integration of geomorphological, geophysical and geotechnical data to define the 3D morpho-structure of the La Valette mudslide (Ubaye Valley, French Alps). In: Malet, J.P., Remaître, A., Boogard, T. (Eds.), Proceedings of the International Conference on Landslide Processes: From Geomorphologic Mapping to Dynamic Modelling, Strasbourg, CERG Editions, pp. 203–208.
Travelletti, J., Sailhac, P., Malet, J.-P., Grandjean, G., Ponton, J., 2012. Hydrological response of weathered clay-shale slopes: water infiltration monitoring with time-lapse electrical resistivity tomography. Hydrol. Process. 26 (14), 2106–2119.
Travelletti, J., Malet, J.-P., Samyn, K., Grandjean, G., Jaboyedoff, M., 2013. Control of landslide retrogression by discontinuities: evidence by the integration of airborne- and ground-based geophysical information. Landslides 10 (1), 37–54.
Ward, S.H., 1988. The Resistivity and Induced Polarization Methods: In Symposium on the Application of Geophysics to Engineering and Environmental Problems 1988. Society of Exploration Geophysicists, pp. 109–250.
Waxman, M.H., Smits, L.J.M., 1968. Electrical conductivities in oil-bearing shaly sands. Soc. Pet. Eng. J. 8 (02), 107–122.
Weigand, M., Flores Orozco, A., Kemna, A., 2017. Reconstruction quality of SIP parameters in multi-frequency complex resistivity imaging: near surface. Geophysics 15 (2), 187–199.
Zhao, Y., Zimmermann, E., Huisman, J.A., Treichel, A., Wolters, B., van Waasen, S., Kemna, A., 2013. Broadband EIT borehole measurements with high phase accuracy using numerical corrections of electromagnetic coupling effects. Meas. Sci. Technol. 24 (8), 085005.
Zimmermann, E., Kemna, A., Berwix, J., Glaas, W., Münch, H.M., Huisman, J.A., 2008. A high-accuracy impedance spectrometer for measuring sediments with low polarizability. Meas. Sci. Technol. 19 (10), 105603.